

Deep Multi-Magnification Networks for Multi-Class Breast Cancer Image Segmentation

David Joon Ho, *Member, IEEE*, Dig V. K. Yarlagadda, Timothy M. D'Alfonso, Matthew G. Hanna, Anne Grabenstetter, Peter Ntiamoah, Edi Brogi, Lee K. Tan, and Thomas J. Fuchs

Abstract—Breast carcinoma is one of the most common cancers for women in the United States. Pathologic analysis of surgical excision specimens for breast carcinoma is important to evaluate the completeness of surgical excision and has implications for future treatment. This analysis is performed manually by pathologists reviewing histologic slides prepared from formalin-fixed tissue. Digital pathology has provided means to digitize the glass slides and generate whole slide images. Computational pathology enables whole slide images to be automatically analyzed to assist pathologists, especially with the advancement of deep learning. The whole slide images generally contain giga-pixels of data, so it is impractical to process the images at the whole-slide-level. Most of the current deep learning techniques process the images at the patch-level, but they may produce poor results by looking at individual patches with a narrow field-of-view at a single magnification. In this paper, we present Deep Multi-Magnification Networks (DMMNs) to resemble how pathologists analyze histologic slides using microscopes. Our multi-class tissue segmentation architecture processes a set of patches from multiple magnifications to make more accurate predictions. For our supervised training, we use partial annotations to reduce the burden of annotators. Our segmentation architecture with multi-encoder, multi-decoder, and multi-concatenation outperforms other segmentation architectures on breast datasets and can be used to facilitate pathologists' assessments of breast cancer.

Index Terms—Breast Cancer, Computational Pathology, Multi-Class Image Segmentation, Deep Multi-Magnification Network, Partial Annotation

I. INTRODUCTION

Breast carcinoma is the most common cancer to be diagnosed and the second leading cause of cancer death for women in the United States [1]. Approximately 12% of women in the United States will be diagnosed with breast cancer during their lifetime [2]. Pathologists diagnose breast carcinoma based on a variety of morphologic features including tumor growth pattern and nuclear cytologic features. Pathologic assessment of breast tissue dictates the clinical management of the patient and provides prognostic information. Breast tissue from a variety of biopsies and surgical specimens is evaluated by

pathologists. For example, patients with early-stage breast cancer often undergo breast-conserving surgery, or lumpectomy, which removes a portion of breast tissue containing the cancer [3]. To determine the completeness of the surgical excision, the edges of the lumpectomy specimen, or margins, are evaluated microscopically by a pathologist. Achieving negative margins (no cancer found touching the margins) is important to minimize the risk of local recurrence of the cancer [4]. Accurate analysis of margins by the pathologist is critical for determining the need for additional surgery. Pathologic analysis of margin specimens involves the pathologist reviewing roughly 20-40 histologic slides per case, and this process can be time-consuming and tedious. With the increasing capabilities of digitally scanning histologic glass slides, computational pathology approaches could potentially improve the efficiency and accuracy of this process by evaluating whole slide images (WSIs) of specimens [5].

Various approaches have been used to analyze WSIs. Most models include localization, detection, classification, and segmentation of objects (i.e. histologic features) in digital slides. Histopathologic features include pattern based identification, such as nuclear features, cellular/stromal architecture, or texture. Computational pathology has been used in nuclei segmentation to extract nuclear features such as size, shape, and relationship between them [6], [7]. Nuclei segmentation is done by adaptive thresholding and morphological operations to find regions where nuclei density is high [8]. A breast cancer grading method can be developed by gland and nuclei segmentation using a Bayesian classifier and structural constraints from domain knowledge [9]. To segment overlapping nuclei and lymphocytes, an integrated active contour based on region, boundary, and shape is presented in [10]. These nuclei-segmentation-based approaches are challenging because shapes of nuclei and structures of cancer regions may have large variations in the tissues captured in the WSIs.

Recently, deep learning, a type of machine learning, has been widely used for automatic image analysis due to the availability of a large training dataset and the advancement of graphics processing units (GPUs) [11]. Deep learning models composed of deep layers with non-linear activation functions enable to learn more sophisticated features. Especially, convolutional neural networks (CNNs) learning spatial features in images have shown outstanding achievements in image classification [12], object detection [13], and semantic segmentation [14]. Fully Convolutional Network (FCN) in [14] developed for semantic segmentation, also known as pixel-wise classification, can understand location, size, and shape

Manuscript received October 28, 2019. This work was supported by the Warren Alpert Foundation Center for Digital and Computational Pathology at Memorial Sloan Kettering Cancer Center and the NIH/NCI Cancer Center Support Grant P30 CA008748.

David Joon Ho, Dig V. K. Yarlagadda, Timothy M. D'Alfonso, Matthew G. Hanna, Anne Grabenstetter, Peter Ntiamoah, Edi Brogi, Lee K. Tan, and Thomas J. Fuchs are with Department of Pathology, Memorial Sloan Kettering Cancer Center, New York, NY 10065 USA. Thomas J. Fuchs is also with Weill Cornell Graduate School for Medical Sciences, New York, NY 10065 USA. (email: hod@mskcc.org; yarlagad@mskcc.org; dalfonst@mskcc.org; hannam@mskcc.org; grabensa@mskcc.org; ntiamoap@mskcc.org; brogie@mskcc.org; tanl@mskcc.org; fuchst@mskcc.org)

of objects in images. FCN is composed of an encoder and a decoder, where the encoder extracts low-dimensional features of an input image and the decoder utilizes the low-dimensional features to produce segmentation predictions. Semantic segmentation has been used on medical images to automatically segment biological structures. For example, U-Net [15] is used to segment cells in microscopy images. U-Net architecture has concatenations transferring feature maps from an encoder to a decoder to preserve spatial information. This architecture has shown more precise segmentation predictions on biomedical images.

Deep learning has recently received high attention in the computational pathology community [16], [17], [18]. Investigators have shown automated identification of invasive breast cancer detection in WSIs by using a simple 3-layer CNN [19]. A method of classifying breast tissue slides to invasive cancer or benign by analyzing stroma regions using CNNs is described in [20]. More recently, a multiple-instance-learning-based CNN achieves 100% sensitivity where the CNN is trained by 44,732 WSIs from 15,187 patients [21]. The availability of public pathology datasets contributes to develop many deep learning approaches for computational pathology. For example, a breast cancer dataset to detect lymph node metastases was released for the CAMELYON challenges [22], [23] and several deep learning techniques to analyze breast cancer datasets are developed [24], [25], [26].

One challenge of using deep learning on WSIs is that the size of a single, entire WSI is too large to be processed into GPUs. Images can be downsampled to be processed by pretrained CNNs [27], [28] but critical details needed for clinical diagnosis in WSIs would be lost. To solve this, patch-based approaches are generally used instead of slide-level approaches. Here, patches are extracted from WSIs to be processed by CNNs. A patch-based process followed by a multi-class logistic regression to classify in slide-level is described in [29]. The winner of the CAMELYON16 challenge uses the Otsu thresholding technique [30] to extract tissue regions and trains a patch-based model to classify tumor and non-tumor patches [24]. To increase the performance, class balancing between tumor and non-tumor patches and data augmentation techniques such as rotation, flip, and color jittering are used in [25]. The winner of the CAMELYON17 challenge additionally develops patch-overlapping strategy for more accurate predictions [26]. In [31], a patch is processed with an additional larger patch including border regions in the same magnification to segment subtypes in breast WSIs. Alternatively, Representation-Aggregation CNNs to aggregate features generated from patches in WSIs are developed to share representations between patches [32], [33]. Patch-based approaches are not realistic because (1) pathologists do not look at slides in patch-level with a narrow field-of-view and (2) they switch zoom levels frequently to see slides in multiple magnifications to accurately analyze them.

To develop more realistic CNNs, it is required to input a set of patches in multiple magnifications to increase the field-of-view and provide more information from other magnifications. Figure 1 shows the difference between a Deep Single-Magnification Network (DSMN) and a Deep Multi-

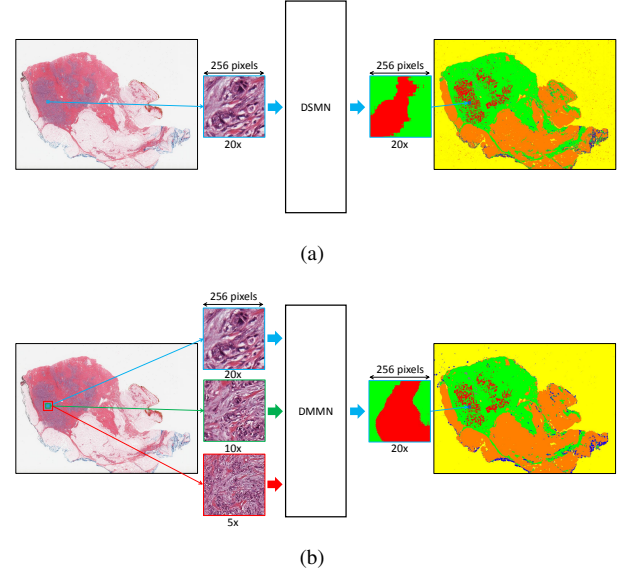


Fig. 1. Comparison between a Deep Single-Magnification Network (DSMN) and a Deep Multi-Magnification Network (DMMN). (a) A Deep Single-Magnification Network only look at a patch from a single magnification with limited field-of-view. (b) A Deep Multi-Magnification Network can look at a set of patches from multiple magnifications to have wider field-of-view.

Magnification Network (DMMN). An input to a DSMN in Figure 1(a) is a single patch with size of 256×256 pixels in a single magnification of 20x which limits a field-of-view. An input to a DMMN in Figure 1(b) is a set of patches with size of 256×256 pixels in multiple magnifications in 20x, 10x, and 5x allowing a wider field-of-view. DMMN can mimic how pathologists look at slides using a microscope by providing multiple magnifications in a wider field-of-view and this can produce more accurate analysis.

There are several works using multiple magnifications to analyze whole slide images. A binary segmentation CNN to segment tumor regions in the CAMELYON dataset [22] is described in [34]. In this work, four encoders for different magnifications are implemented but only one decoder is used to generate the final segmentation predictions. More recently, a CNN architecture composed of three expert networks for different magnifications, a weighting network to automatically select weights to emphasize specific magnifications based on input patches, and an aggregating network to produce final segmentation predictions is developed in [35]. Here, intermediate feature maps are not shared between the three expert networks which can limit utilizing feature maps from multiple magnifications.

In this paper, we present a Deep Multi-Magnification Network (DMMN) to accurately segment multiple subtypes in images of breast tissue, with the goal to identify breast cancer found in specimens. Our DMMN architecture has multiple encoders, multiple decoders, and multiple concatenations between decoders to have richer feature maps in intermediate layers. To train our DMMN, we partially annotate WSIs, similarly done as [36], to reduce the burden of annotations. Our DMMN model trained by our partial annotations can learn not only features of each subtype, but also morphological

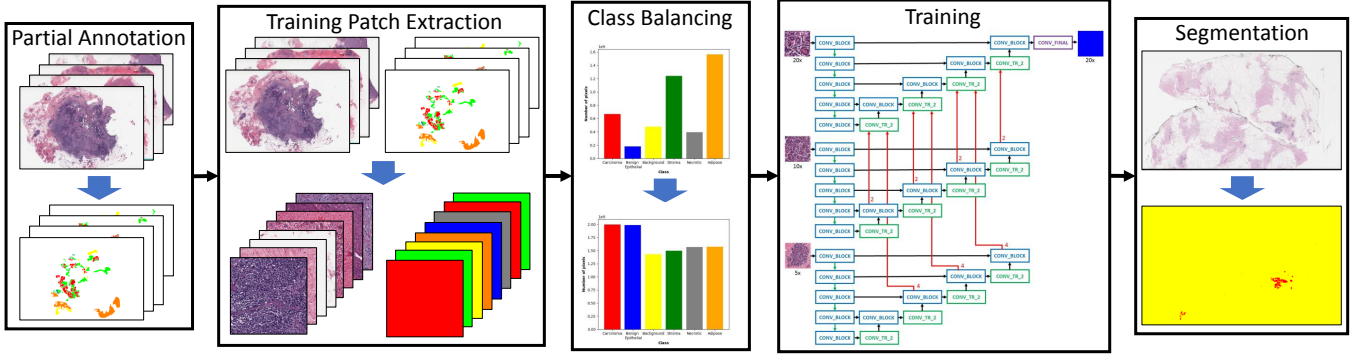


Fig. 2. Block diagram of the proposed method with our Deep Multi-Magnification Network. The first step of our method is to partially annotate training whole slide images. After extracting training patches from the partial annotations and balancing the number of pixels between classes, our Deep Multi-Magnification Network is trained. The trained network is used for multi-class tissue segmentation of whole slide images.

relationship between subtypes, which leads to outstanding segmentation performance. We test our multi-magnification model on two breast datasets and observe that our model consistently outperforms other architectures. Our method can be used to automatically segment cancer regions on breast images to assist in diagnosis of patients' status and to decide future treatments. The main contributions of our work are the followings: (1) We develop Deep Multi-Magnification Networks combining feature maps in various magnification for more accurate segmentation predictions, and (2) We introduce partial annotations to save annotation time for pathologists and still achieve high performance.

II. PROPOSED METHOD

Figure 2 shows the block diagram of our proposed method. Our goal is to segment cancer regions on breast images using our Deep Multi-Magnification Network (DMMN). First of all, manual annotations is done on the training dataset with C classes. Note this annotation is done partially for an efficient and fast process. To train our multi-class segmentation DMMN, patches are extracted from whole slide images and the corresponding annotations. Before training our DMMN with the extracted patches, we use elastic deformation [15], [37] to multiply patches belonging to rare classes to balance the number of annotated pixels between classes. After the training step is done, the model can be used for multi-class segmentation of breast cancer images. We have implemented our system in PyTorch [38].

A. Partial Annotation

A large set of annotations is needed for supervised learning, but this is generally an expensive step requiring pathologists' time and effort. Especially, due to giga-pixel scale of image size, exhaustive annotation to label all pixels in whole slide images is not practical. Many works are done using public datasets such as CAMELYON datasets [22], [23] but public datasets are designed for specific application and may not be generalized to other applications. To segment multiple tissue subtypes on our breast training dataset, we partially annotate images.

For partial annotations, we (1) avoided annotating close boundary regions between subtypes while minimizing the thickness of these unlabeled regions and (2) annotated the entire subtype components without cropping. Exhaustive annotations, especially on boundary regions, without any overlapping portions and subsequent inaccurate labeling can be challenging given the regions merge into each other seamlessly. Additionally, the time required for complete, exhaustive labeling is immense. By minimizing the thickness of these unlabeled boundary regions, our CNN model trained by our partial annotation can learn the spatial relationships between subtypes and generate precise segmentation boundaries. This is different from the partial annotation done in [36] where annotated regions of different subtypes were too widely spaced and thus unsuitable for training spatial relationships between them. The work in [36] also suggests exhaustive annotation in subregions of whole slide images to reduce annotation efforts, but if the subtype components are cropped the CNN model cannot learn the growth pattern of the different subtypes. In this work, we annotated each subtype component entirely to let our CNN model learn the growth pattern of all subtypes. Figure 3 shows an example of our partial annotations where an experienced pathologist can spend approximately 30 minutes to partially annotate one whole slide image. Note white regions in Figure 3(b) are unlabeled.

B. Training Patch Extraction

Whole slide images are generally too large to process in slide-level using convolutional neural networks. For example, the dimension of the smallest WSI we have is 43,824 pixels by 31,159 pixels which is more than 1.3 billion pixels. To analyze WSIs, patch-based methods are used where patches extracted from an image is processed by a CNN and then the outputs are combined for slide-level analysis. One limitation of the patch-based methods is that they do not mimic pathologists, who switch zoom levels while examining a slide. In contrast, patch-based methods only look at patches in a single magnification with a limited field-of-view.

To resemble what pathologists do with a microscope, we extract a set of multi-magnification patches to train our DMMN. In this work, we set the size of a target patch to be analyzed in

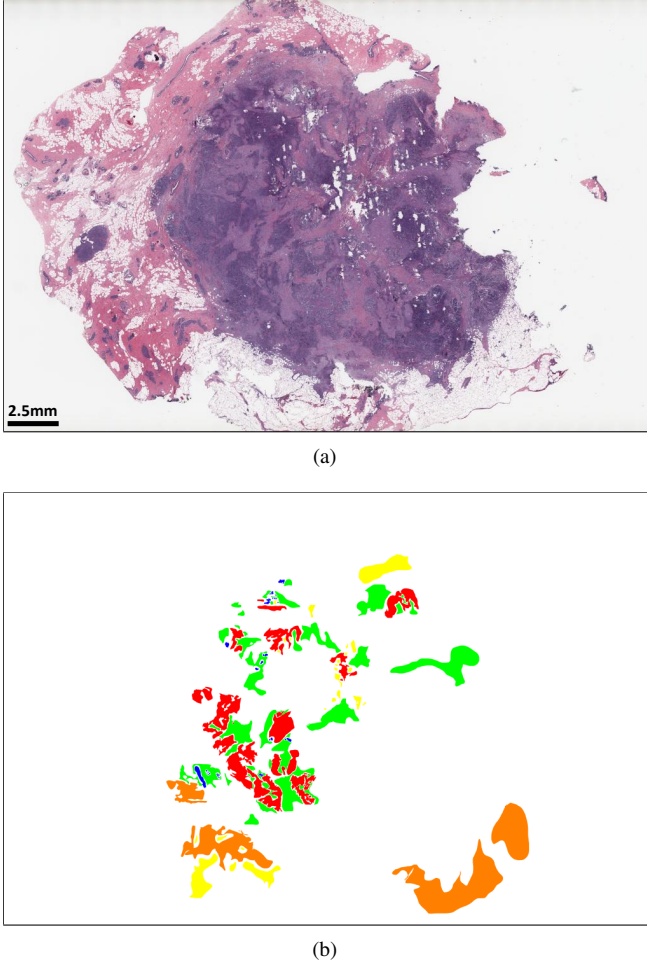


Fig. 3. An example of partial annotation. (a) A whole slide image from a breast cancer dataset. (b) A partially annotated image of the whole slide image in (a) where multiple tissue subtypes are annotated in distinct colors and white regions are unlabeled.

a WSI be 256×256 pixels in 20x magnification. To analyze the target patch, an input patch with size of 1024×1024 pixels in 20x is extracted from the image where the target patch is located at the center of the input patch. From this input patch, a set of three multi-magnification patches is extracted. The first patch is extracted from the center of the input patch with size of 256×256 pixels in 20x, which is the same location and magnification with the target patch. The second patch is extracted from the center of the input patch with size of 512×512 pixels and downsampled by a factor of 2 to become size of 256×256 pixels in 10x. Lastly, the third patch is generated by downsampling the input patch by a factor of 4 to become size of 256×256 pixels in 5x. The set of three patches in different magnifications becomes the input to our DMMN to segment cancer in the target patch with size of 256×256 pixels. Input patches are extracted from training images if more than 1% of pixels in the corresponding target patches are annotated. The stride to x and y -directions is 256 pixels to avoid overlapping target patches.

C. Class Balancing

Class balancing is a prerequisite step for training CNNs for accurate performance [39]. When the number of training patches in one class dominates the number of training patches in another class, CNNs cannot properly learn features from the minor class. In this work, class imbalance is observed in our annotations. For example, the number of annotated pixels in carcinoma regions dominates the number of annotated pixels in benign epithelial regions. To balance between classes, elastic deformation [15], [37] is used to multiply training patches belonging to minor classes.

Elastic deformation is widely used as a data augmentation technique in biomedical images due to the squiggling shape of biological structures. To perform elastic deformation on a patch, a set of grid points in the patch is selected and displaced randomly by a normal distribution with a standard deviation of σ . According to the displacements of the grid points, all pixels in the patch are displaced by bicubic interpolation. In this work, we set the grid points by 17×17 and $\sigma = 4$.

The number of patches to be multiplied needs to be carefully selected to balance the number of pixels between classes. Here, we define a rate of elastic deformation for a class c , denoted as r_c , to be the number of patches to be multiplied for the class c and a class order to decide the order of classes when multiplying patches. The rate can be selected based on the number of pixels in each class. The rate is a non-negative integer and elastic deformation is not performed if the rate is 0. The class order can be decided based on applications. For example, if one desires an accurate segmentation on carcinoma regions, then a class of carcinoma would have a higher order than other classes. To multiply patches, each patch needs to be classified to a class c if the patch contains a pixel label classified to c . If a patch contains pixels in multiple classes, a class with a higher class order becomes the class of the patch. After patches are classified, r_c number of patches will be multiplied for each patch in class c using elastic deformation. Once class balancing is done, all patches are used to train CNNs.

D. CNN Architectures

Figure 4 shows architectures of a Deep Single-Magnification Network (DSMN) and Deep Multi-Magnification Networks (DMMNs) for multi-class tissue segmentation. Note the size of input patches is 256×256 pixels and the size of an output prediction is 256×256 pixels. CONV_BLOCK contains two sets of a convolutional layer with kernel size of 3×3 with padding of 1 followed by a rectified linear unit (ReLU) activation function in series. CONV_TR_ u contains a transposed convolutional layer followed by the ReLU activation function where u is an upsampling rate. Note CONV_TR_4 is composed of two CONV_TR_2 in series. CONV_FINAL contains a convolutional layer with kernel size of 3×3 with padding of 1, the ReLU activation function, and a convolutional layer with kernel size of 1×1 to output C channels. The final segmentation predictions are produced using the softmax operation. Green arrows are max-pooling operations by a factor of 2 and red arrows are center-crop

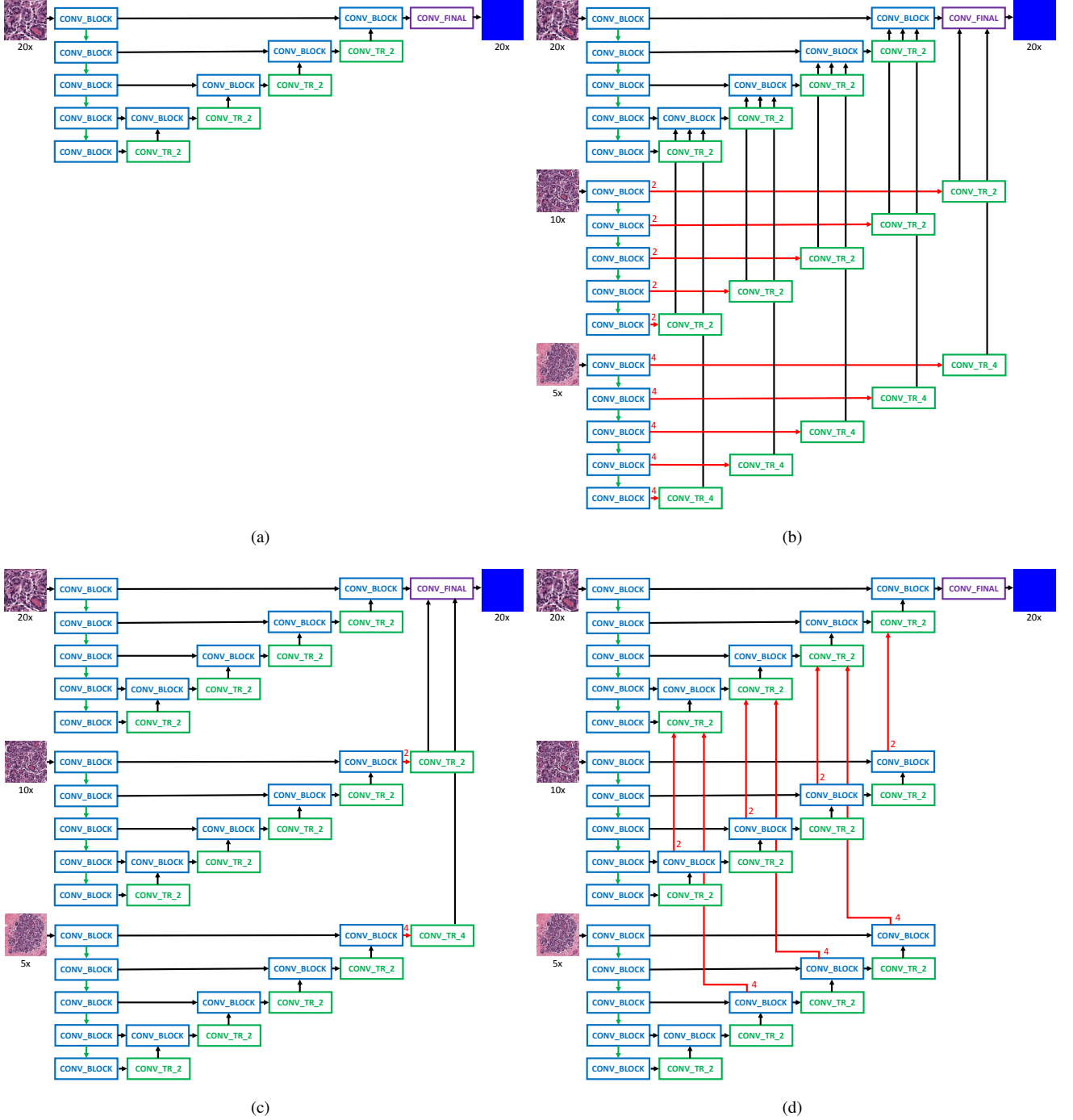


Fig. 4. CNN architectures for multi-class tissue segmentation of a Deep Single-Magnification Network (DSMN) in (a) and Deep Multi-Magnification Networks (DMMNs) in (b)-(d). (a) Single-Encoder Single-Decoder (DSMN-S2) is a DSMN architecture utilizing a patch from a single magnification to generate a segmentation prediction patch. (b) Multi-Encoder Single-Decoder (DMMN-MS) is a DMMN architecture utilizing multiple patches in various magnifications but it has only one decoder to generate a segmentation prediction patch. (c) Multi-Encoder Multi-Decoder Single-Concatenation (DMMN-M2S) is a DMMN architecture utilizing multiple patches in various magnifications but feature maps are only concatenated at the final layer to generate a segmentation prediction patch. (d) Our proposed Multi-Encoder Multi-Decoder Multi-Concatenation (DMMN-M3) is a DMMN architecture utilizing multiple patches in various magnifications and feature maps are concatenated during intermediate layers to enrich feature maps in the decoder of the highest magnification.

operations where cropping rates are written in red. The center-crop operations crop the center regions of feature maps in all channels by the cropping rate to fit the size and magnification of feature maps for the next operation. During the center-crop operations, the width and height of the cropped feature maps become a half and a quarter of the width and height of the

input feature maps if the cropping rate is 2 and 4, respectively.

The Single-Encoder Single-Decoder (DSMN-S2) architecture in Figure 4(a) uses a single magnification patch in 20x to produce the corresponding segmentation predictions. Note that this implementation is the same as U-Net [15] except the number of channels is reduced by a factor of 2. The

Multi-Encoder Single-Decoder (DMMN-MS) architecture in Figure 4(b), motivated by the work in [34], uses multiple encoders for 20x, 10x, and 5x magnifications, but only uses a single decoder to produce segmentation predictions. The Multi-Encoder Multi-Decoder Single-Concatenation (DMMN-M2S) architecture in Figure 4(c), motivated by the work in [35], has multiple encoders and the corresponding decoders for 20x, 10x, and 5x magnifications, but the concatenation is done only at the end of the encoder-decoder pairs. Note that the weighting CNN in [35] is excluded for a fair comparison with other architectures. Lastly, our proposed architecture, the Multi-Encoder Multi-Decoder Multi-Concatenation (DMMN-M3) architecture in Figure 4(d), has multiple encoders and decoders and has concatenations between multiple layers in the decoders to enrich feature maps in the 20x decoder.

E. CNN Training

The balanced set of patches from Section II-C is used to train our multi-class segmentation CNNs. We used a weighted cross entropy as our training loss function with N pixels in a patch and C classes:

$$L(t_c^{gt}, t_c^{pred}) = -\frac{1}{N} \sum_{p=1}^N \sum_{c=1}^C w_c t_c^{gt}(p) \log t_c^{pred}(p) \quad (1)$$

where t_c^{gt} and t_c^{pred} are two-dimensional groundtruth and segmentation predictions for a class c , respectively. $t_c^{gt}(p)$ is a binary groundtruth value for a class c at a pixel location p , either 0 or 1, and $t_c^{pred}(p)$ is a segmentation prediction value for a class c at a pixel location p , between 0 and 1. In Equation 1, a weight for class c , w_c is defined as

$$w_c = 1 - \frac{N_c}{\sum_c N_c} \quad (2)$$

where N_c is the number of pixels for class c in a training set. Note unlabeled pixels do not contribute to the training loss function. We use stochastic gradient descent (SGD) with a learning rate of 5×10^{-5} , a momentum of 0.99, and a weight decay of 10^{-4} is used for 20 epochs for optimization. A CNN model with the highest mean intersection-over-union (mIOU) on validation images is selected as the final model. During training, data augmentation using rotation, vertical and horizontal flip, brightness, contrast, and color jittering is used.

F. Multi-Class Segmentation

Multi-class tissue segmentation on breast images can be done using the trained CNN. The final label in each pixel is selected as a class which has the largest prediction value among the C classes. An input patch with size of 1024×1024 pixels is extracted from a whole slide image to generate a set of three patches with size of 256×256 pixels in 20x, 10x, and 5x magnifications by the process described in Section II-B. The set of three patches is processed by our trained CNN. The segmentation predictions with size of 256×256 pixels are located at the center location of the input patch. Input patches are extracted from the top-left corner of the WSI with a stride of 256 pixels in x and y directions to process the

entire WSI. Zero-padding is done to extract input patches on the boundary of WSIs. The Otsu thresholding technique [30] can be used before extracting patches as optional to remove background regions to speed up the segmentation process.

III. EXPERIMENTAL RESULTS

Our goal is to segment carcinoma regions on our breast datasets. We used a Triple-Negative Breast Cancer (TNBC) dataset containing large invasive ductal carcinoma (IDC) regions to train our CNN model and a breast margin dataset containing IDC and ductal carcinoma in situ (DCIS) of various histologic grades as an additional testing set. All whole slide images in the TNBC dataset and the breast margin dataset were hematoxylin and eosin (H&E) stained and digitized from Memorial Sloan Kettering Cancer Center. The TNBC dataset was scanned by Aperio XT where microns per pixel (MPP) in 20x is 0.4979 and the breast margin dataset was scanned by Aperio AT2 where MPP in 20x is 0.5021.

We partially annotated 38 images from the TNBC dataset. We split the TNBC dataset as 26 training images, 6 validation images, and 6 testing images. We have 6 classes ($C = 6$) in our TNBC dataset which are carcinoma, benign epithelial, background, stroma, necrotic, and adipose. Note that background is defined as regions which are not tissue. In our work, 5.48% of pixels of whole slide images were annotated. To balance the number of annotated pixels between classes, we empirically set $r_2 = 10$, $r_1 = 2$, $r_5 = 3$, $r_3 = 1$, $r_4 = 0$, and $r_6 = 0$ where r_1, r_2, r_3, r_4, r_5 , and r_6 are rates of elastic deformation of carcinoma, benign epithelial, background, stroma, necrotic, and adipose, respectively. Benign epithelial was selected as the highest class order followed by carcinoma, necrotic, and background, because we want to accurately segment carcinoma regions and separate benign epithelial to reduce false segmentation. Figure 5 shows the number of annotated pixels between classes are balanced using elastic deformation. Using a single NVIDIA GeForce GTX TITAN X GPU, our training process took approximately 3 days.

We processed the testing images of the TNBC dataset using a Deep Single-Magnification Network (DSMN) and Deep Multi-Magnification Networks (DMMNs). Figures 6 and 7 show multi-class segmentation predictions of the Single-Encoder Single-Decoder (DSMN-S2) architecture, the Multi-Encoder Single-Decoder (DMMN-MS) architecture, the Multi-Encoder Multi-Decoder Single-Concatenation (DMMN-M2S) architecture, and our proposed Multi-Encoder Multi-Decoder Multi-Concatenation (DMMN-M3) architecture, both slide-level and 10x magnification. To be able to analyze tumor microenvironment, various subtypes are labeled in distinct colors such as carcinoma in red, benign epithelial in blue, background in yellow, stroma in green, necrotic in gray, and adipose in orange. Note that white regions in Figures 6(b), (h) and 7(b), (h) are unlabeled. The Otsu thresholding technique [30] is not used for segmentation on the TNBC dataset because we observed that adipose regions are predicted as background due to their pixel intensities. Without the Otsu thresholding technique, segmentation on one WSI took approximately 15 minutes using the single GPU. It is observed that DSMN-S2 does not produce accurate boundaries between subtypes

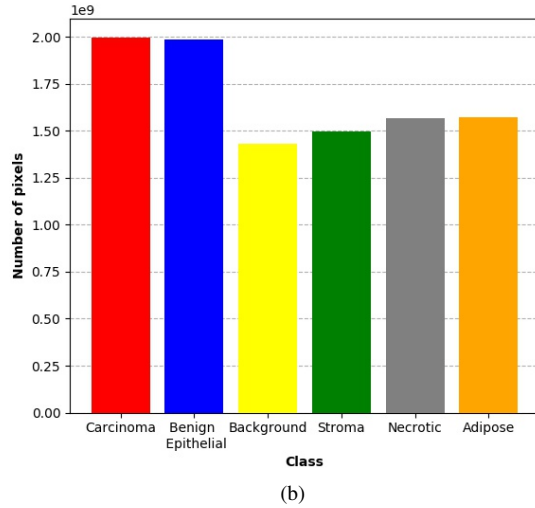
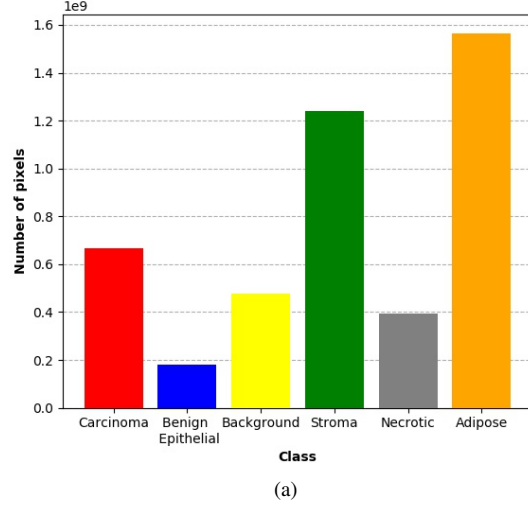


Fig. 5. Class balancing using elastic deformation in the training breast dataset. (a) Number of annotated pixels between classes before elastic deformation. (b) Number of annotated pixels between classes after elastic deformation.

because the field-of-view is narrow to make accurate segmentation predictions. DMMN-MS sometimes cannot distinguish between carcinoma and benign epithelial. DMMN-M2S and DMMN-M3 produce accurate segmentation predictions for the TNBC images.

We processed 10 breast margin images using the same multi-class segmentation models. All carcinoma regions were exhaustively annotated for a precise evaluation. Figure 8 shows segmentation predictions on a breast margin image, both slide-level and 10x magnification. Pathologists are interested in detecting cancers on margin images as a screening tool to evaluate lumpectomy, so cancer regions are highlighted in red and non-cancer regions including benign epithelial, background, stroma, necrotic, and adipose are labeled in yellow. The Otsu thresholding technique [30] was used to extract patches only on foreground regions of the whole slide images to reduce processing time because we are interested in segmenting cancer regions on breast margin images. With the

Otsu thresholding technique, segmentation on one WSI took approximately 2 minutes using the single GPU. DSMN-S2 still produces segmentation predictions with inaccurate boundary. We observe that large non-cancer regions are falsely segmented as cancer by DMMN-M2S. DMMN-MS and DMMN-M3 produce accurate segmentation on carcinoma regions for the breast margin images.

We evaluated our predictions numerically using intersection-over-union (IOU), recall, and precision. IOU, recall, and precision are defined as the followings:

$$IOU = \frac{N_{TP}}{N_{TP} + N_{FP} + N_{FN}} \quad (3)$$

$$Recall = \frac{N_{TP}}{N_{TP} + N_{FN}} \quad (4)$$

$$Precision = \frac{N_{TP}}{N_{TP} + N_{FP}} \quad (5)$$

where N_{TP} , N_{FP} , and N_{FN} are the number of pixels for true-positive, false-positive, and false-negative, respectively. Table I shows IOU, recall, and precision values on the TNBC dataset. Note that the evaluations in Table I were done using our partially-annotated TNBC images. We observe that our proposed architecture (DMMN-M3) outperforms other architectures. Especially, separating carcinoma and benign epithelial is known to be challenging due to similar morphological patterns but our proposed method has the highest IOU for both carcinoma and benign epithelial. Table II shows IOU, recall, and precision on our four models on carcinoma regions on the breast margin dataset. Our model was trained on TNBC dataset and we kept aside breast margin images for our testing set. Note only 0.188% of pixels in our 10 breast margin images were exhaustively labeled as carcinoma. DSMN-S2 and DMMN-M2S have low precision values because many non-cancer regions are segmented as cancer. DMMN-MS can successfully segment carcinoma regions on the breast margin images but it does not segment well on the TNBC dataset. Our numerical analysis shows that our proposed DMMN-M3 model has good carcinoma segmentation performance on both datasets, proving that our model can generalize successfully on unseen datasets.

IV. CONCLUSIONS

We described a Deep Multi-Magnification Network (DMMN) for an accurate multi-class tissue segmentation on whole slide images. Our model is trained by partially-annotated images to reduce time and effort for annotators. Although the annotation was partially done, our model was able to learn not only spatial characteristics within a class but also spatial relationship between classes. Our DMMN architecture see all 20x, 10x, and 5x magnifications to have a wider field-of-view to make more accurate predictions. We were able to improve previous DMMNs by transferring intermediate feature maps in 10x and 5x decoders to the 20x decoder to enrich feature maps. Our implementation achieved outstanding segmentation performance on multiple breast dataset. Especially, automatic cancer segmentation on breast margin images can be used to decide patients' future

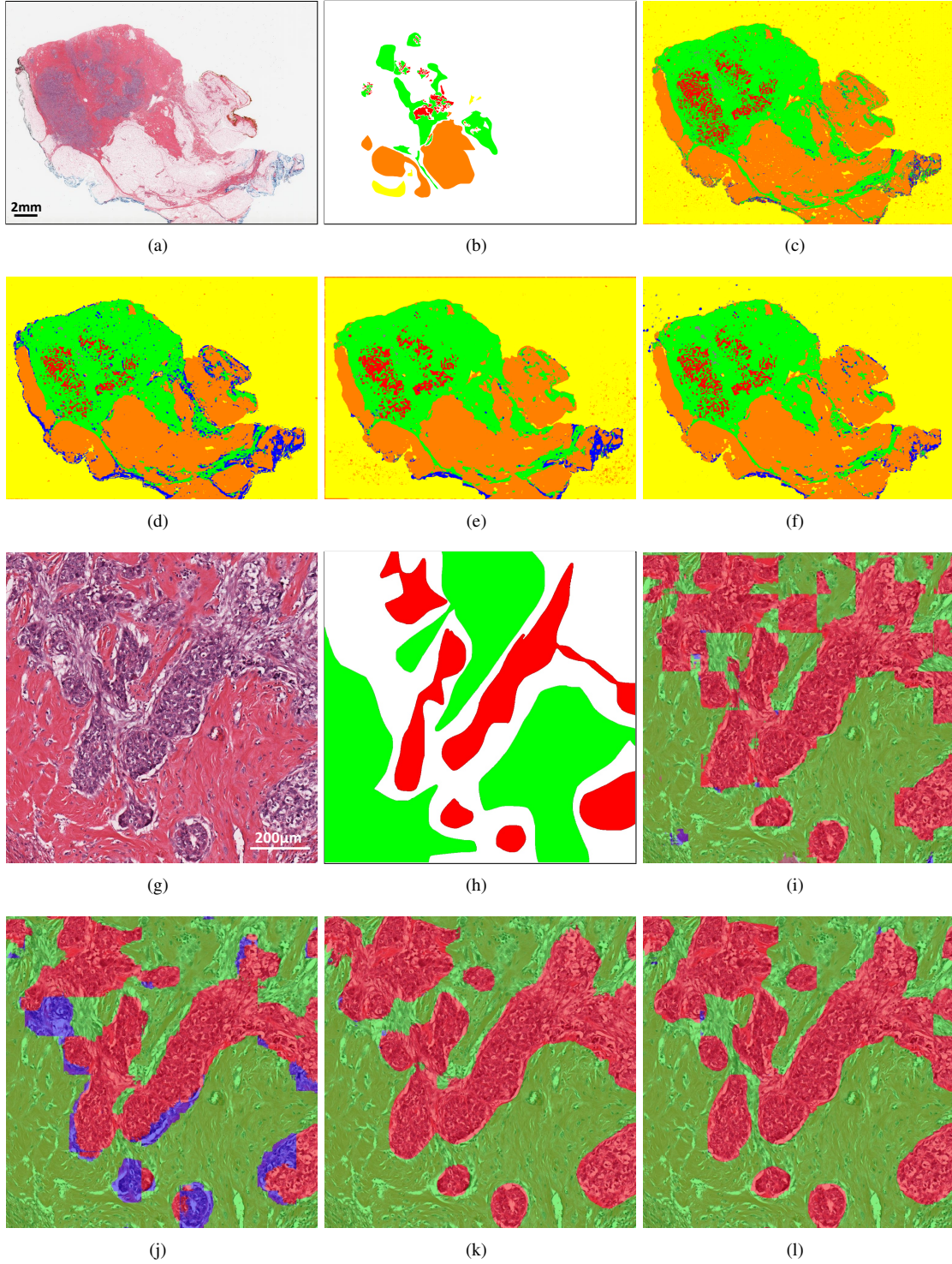


Fig. 6. Segmentation predictions on the TNBC dataset from a Deep Single-Magnification Network (DSMN) and Deep Multi-Magnification Networks (DMMNs). (a)-(f) are thumbnail versions of a whole slide image and (g)-(l) are zoom-in images with size of 1024×1024 pixels in magnification of 10x. (a) and (g) are original image, (b) and (h) are partial annotations, (c) and (i) are segmentation predictions using the Single-Encoder Single Decoder (DSMN-S2) architecture, (d) and (j) are segmentation predictions using the Multi-Encoder Single Decoder (DMMN-MS) architecture, (e) and (k) are segmentation predictions using the Multi-Encoder Multi-Decoder Single-Concatenation (DMMN-M2S) architecture, and (f) and (l) are segmentation predictions using our proposed Multi-Encoder Multi-Decoder Multi-Concatenation (DMMN-M3) architecture.

treatment. We observed that our model may not successfully segment low-grade well-differentiated carcinomas presented in breast images because it was mainly trained by invasive ductal carcinomas. In the future, we plan to develop more accurate

DMMN model where various cancer structures are included during training.

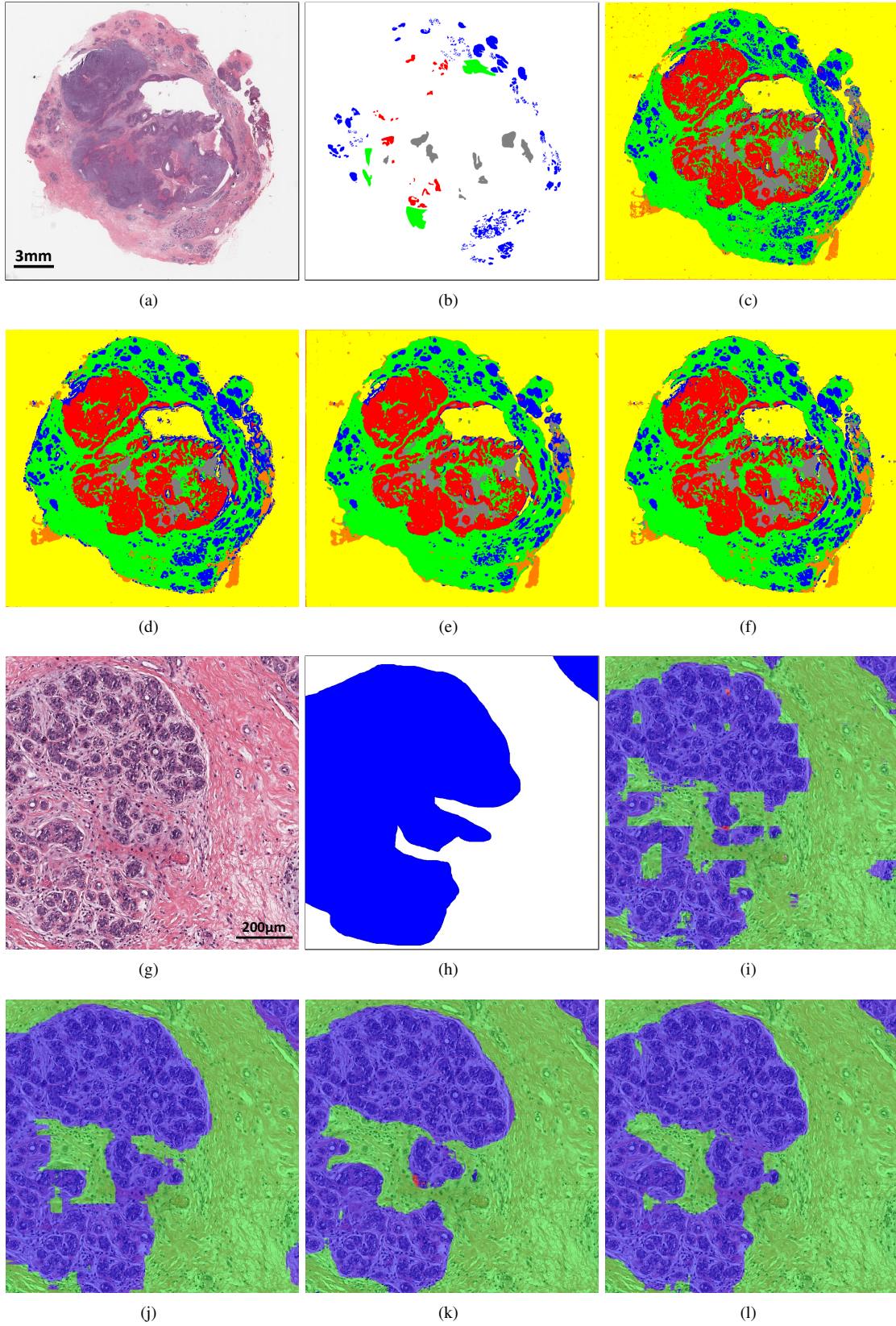


Fig. 7. Segmentation predictions on the TNBC dataset from a Deep Single-Magnification Network (DSMN) and Deep Multi-Magnification Networks (DMMNs). (a)-(f) are thumbnail versions of a whole slide image and (g)-(l) are zoom-in images with size of 1024×1024 pixels in magnification of 10x. (a) and (g) are original image, (b) and (h) are partial annotations, (c) and (i) are segmentation predictions using the Single-Encoder Single Decoder (DSMN-S2) architecture, (d) and (j) are segmentation predictions using the Multi-Encoder Single Decoder (DMMN-MS) architecture, (e) and (k) are segmentation predictions using the Multi-Encoder Multi-Decoder Single-Concatenation (DMMN-M2S) architecture, and (f) and (l) are segmentation predictions using our proposed Multi-Encoder Multi-Decoder Multi-Concatenation (DMMN-M3) architecture.

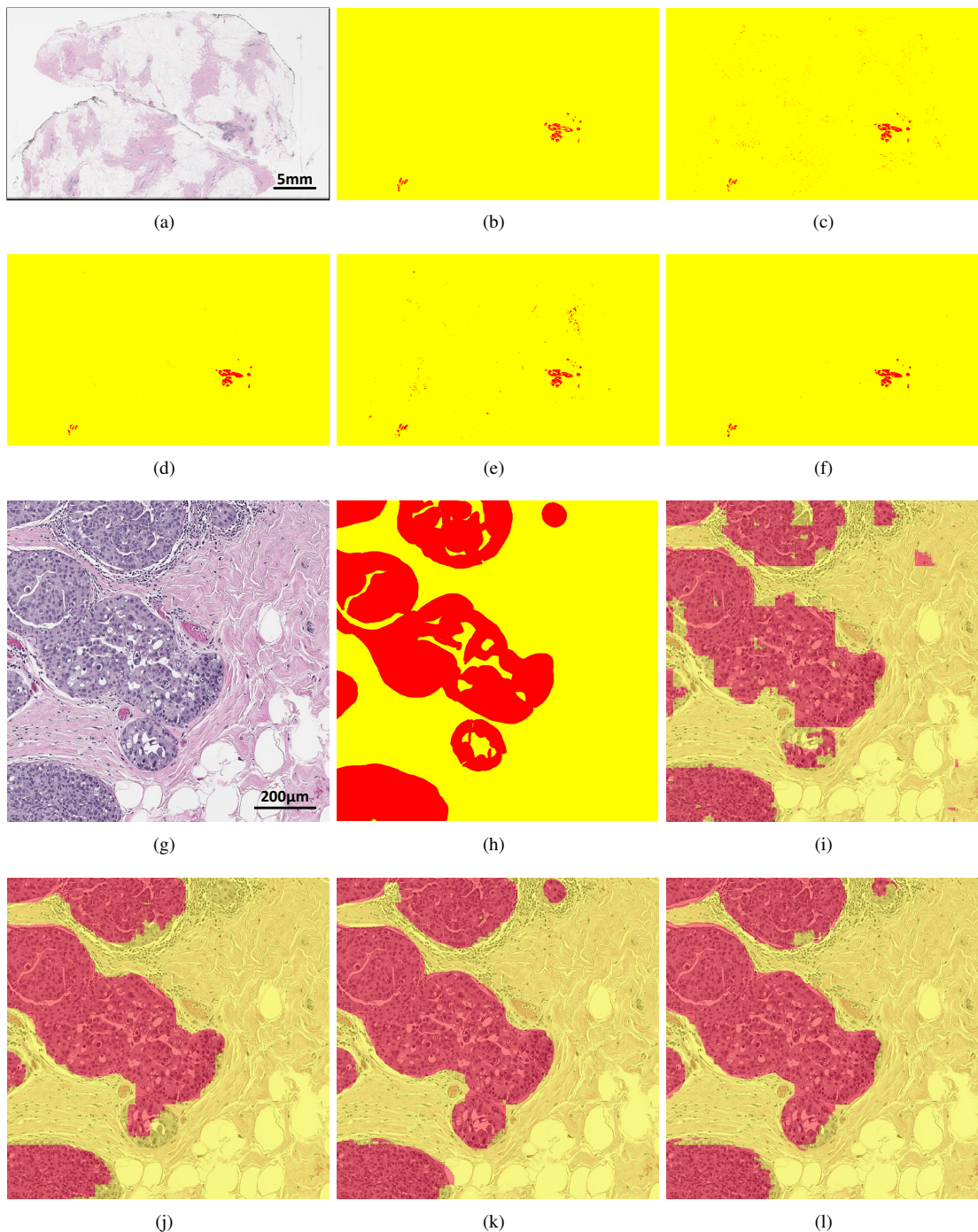


Fig. 8. Segmentation predictions on the breast margin dataset from a Deep Single-Magnification Network (DSMN) and Deep Multi-Magnification Networks (DMMNs). (a)-(f) are thumbnail versions of a whole slide image and (g)-(l) are zoom-in images with size of 1024×1024 pixels in magnification of 10x. (a) and (g) are original image, (b) and (h) are exhaustive annotations, (c) and (i) are segmentation predictions using the Single-Encoder Single Decoder (DSMN-S2) architecture, (d) and (j) are segmentation predictions using the Multi-Encoder Single Decoder (DMMN-MS) architecture, (e) and (k) are segmentation predictions using the Multi-Encoder Multi-Decoder Single-Concatenation (DMMN-M2S) architecture, and (f) and (l) are segmentation predictions using our proposed Multi-Encoder Multi-Decoder Multi-Concatenation (DMMN-M3) architecture.

V. ACKNOWLEDGMENT

T.J.F. is the Chief Scientific Officer, co-founders and equity holders of Paige.AI. M.G.H. is a consultant for Paige.AI and on the medical advisory board of PathPresenter. D.J.H. and T.J.F. have intellectual property interests relevant to the work that is the subject of this paper. MSK has financial interests

in Paige.AI. and intellectual property interests relevant to the work that is the subject of this paper.

REFERENCES

- [1] F. Bray, J. Ferlay, I. Soerjomataram, R.L. Siegel, L.A. Torre, and A. Jemal, "Global cancer statistics 2018: GLOBOCAN estimates of incidence and mortality worldwide for 36 cancers in 185 countries," *CA*:

TABLE I
INTERSECTION-OVER-UNION (IOU), RECALL, AND PRECISION ON THE TNBC DATASET

		DSMN-S2	DMMN-MS	DMMN-M2S	DMMN-S3
Carcinoma	IOU	0.869	0.895	0.899	0.927
	Recall	0.966	0.955	0.981	0.966
	Precision	0.896	0.934	0.915	0.958
Benign Epithelial	IOU	0.841	0.777	0.864	0.916
	Recall	0.936	0.978	0.951	0.973
	Precision	0.892	0.791	0.904	0.940
Stroma	IOU	0.877	0.909	0.899	0.916
	Recall	0.919	0.940	0.923	0.946
	Precision	0.951	0.965	0.971	0.967
Necrotic	IOU	0.902	0.905	0.929	0.914
	Recall	0.938	0.940	0.972	0.970
	Precision	0.959	0.960	0.954	0.941
Adipose	IOU	0.966	0.979	0.976	0.985
	Recall	0.977	0.985	0.985	0.991
	Precision	0.989	0.993	0.991	0.994
Background	IOU	0.910	0.924	0.919	0.965
	Recall	0.947	0.931	0.924	0.981
	Precision	0.959	0.992	0.994	0.983
Mean	IOU	0.894	0.898	0.914	0.937
	Recall	0.947	0.955	0.956	0.971
	Precision	0.941	0.939	0.955	0.964

TABLE II
INTERSECTION-OVER-UNION (IOU), RECALL, AND PRECISION ON THE BREAST MARGIN DATASET

		DSMN-S2	DMMN-MS	DMMN-M2S	DMMN-S3
Carcinoma	IOU	0.205	0.468	0.341	0.447
	Recall	0.601	0.612	0.566	0.587
	Precision	0.237	0.666	0.462	0.653

- A Cancer Journal for Clinicians*, vol. 68, no. 6, pp. 394–424, November 2018.
- [2] C.E. DeSantis, J. Ma, A. Goding Sauer, L.A. Newman, and A. Jemal, “Breast cancer statistics, 2017, racial disparity in mortality by state,” *CA: A Cancer Journal for Clinicians*, vol. 67, no. 6, pp. 439–448, November 2017.
- [3] T.-A. Moo, L. Choi, C. Culpepper, C. Olcese, A. Heerdt, L. Sclafani, T. A. King, A. S. Reiner, S. Patil, E. Brogi, M. Morrow, and K. J. Van Zee, “Impact of margin assessment method on positive margin rate and total volume excised,” *Annals of Surgical Oncology*, vol. 21, no. 1, pp. 86–92, January 2014.
- [4] I. Gage, S.J. Schnitt, A.J. Nixon, B. Silver, A. Recht, S.L. Troyan, T. Eberlein, S.M. Love, R. Gelman, J.R. Harris, and J.L. Connolly, “Pathologic margin involvement and the risk of recurrence in patients treated with breast-conserving therapy,” *Cancer*, vol. 78, no. 9, pp. 1921–1928, November 1996.
- [5] T. J. Fuchs and J. M. Buhmann, “Computational pathology: Challenges and promises for tissue analysis,” *Computerized Medical Imaging and Graphics*, vol. 35, no. 7, pp. 515–530, October 2011.
- [6] M. N. Gurcan, L. E. Boucheron, A. Can, A. Madabhushi, N. M. Rajpoot, and B. Yener, “Histopathological image analysis: A review,” *IEEE Reviews in Biomedical Engineering*, vol. 2, pp. 147–171, October 2009.
- [7] M. Veta, J. P. W. Pluim, P. J. van Diest, and M. A. Viergever, “Breast cancer histopathology image analysis: A review,” *IEEE Transactions on Biomedical Engineering*, vol. 61, no. 5, pp. 1400–1411, May 2014.
- [8] S. Petushi, F.U. Garcia, M.M. Haber, C. Katsinis, and A. Tozeren, “Large-scale computations on histology images reveal grade-differentiating parameters for breast cancer,” *BMC Medical Imaging*, vol. 6, no. 14, October 2006.
- [9] S. Naik, S. Doyle, S. Agner, A. Madabhushi, M. Feldman, and J. Tomaszewski, “Automated gland and nuclei segmentation for grading of prostate and breast cancer histopathology,” *Proceedings of the IEEE International Symposium on Biomedical Imaging*, pp. 284–287, May 2008, Paris, France.
- [10] S. Ali and A. Madabhushi, “An integrated region-, boundary-, shape-based active contour for multiple object overlap resolution in histological imagery,” *IEEE Transactions on Medical Imaging*, vol. 31, no. 7, pp. 1448–1460, July 2012.
- [11] Y. LeCun, Y. Bengio, and G. Hinton, “Deep learning,” *Nature*, vol. 521, pp. 436–444, May 2015.
- [12] A. Krizhevsky, I. Sutskever, and G. E. Hinton, “ImageNet classification with deep convolutional neural networks,” *Proceedings of the Neural Information Processing Systems*, pp. 1097–1105, December 2012, Lake Tahoe, NV.
- [13] R. Girshick, J. Donahue, T. Darrell, and J. Malik, “Rich feature hierarchies for accurate object detection and semantic segmentation,” *Proceedings of the IEEE Conference on Computer Vision and Pattern Recognition*, pp. 580–587, June 2014, Columbus, OH.
- [14] J. Long, E. Shelhamer, and T. Darrell, “Fully convolutional networks for semantic segmentation,” *Proceedings of the IEEE Conference on Computer Vision and Pattern Recognition*, pp. 3431–3440, June 2015, Boston, MA.
- [15] O. Ronneberger, P. Fischer, and T. Brox, “U-Net: Convolutional networks for biomedical image segmentation,” *Proceedings of the Medical Image Computing and Computer-Assisted Intervention*, pp. 231–241, October 2015, Munich, Germany.
- [16] A. Janowczyk and A. Madabhushi, “Deep learning for digital pathology image analysis: A comprehensive tutorial with selected use cases,” *Journal of Pathology Informatics*, vol. 7, no. 29, July 2016.
- [17] G. Litjens, T. Kooi, B. Ehteshami Bejnordi, A.A.A. Setio, F. Ciompi, M. Ghafoorian, J.A.W.M. van der Laak, B. van Ginneken, and C. I. Sanchez, “A survey on deep learning in medical image analysis,” *Medical Image Analysis*, vol. 42, pp. 60–88, July 2017.
- [18] S. Robertson, H. Azizpour, K. Smith, and J. Hartman, “Digital image analysis in breast pathology from image processing techniques to artificial intelligence,” *Translational Research*, vol. 194, pp. 19–35, April 2018.
- [19] A. Cruz-Roa, H. Gilmore, A. Basavanahally, M. Feldman, S. Ganesan, N.N.C. Shih, J. Tomaszewski, F.A. Gonzalez, and A. Madabhushi, “Accurate and reproducible invasive breast cancer detection in whole-slide images: A deep learning approach for quantifying tumor extent,” *Scientific Reports*, vol. 7, pp. 46450:1–14, April 2017.
- [20] B. Ehteshami Bejnordi, M. Mullooly, R.M. Pfeiffer, S. Fan, P.M. Vacek, D.L. Weaver, S. Herschorn, L.A. Brinton, B. van Ginneken, N. Karssemeijer, A.H. Beck, G.L. Gierach, J.A.W.M. van der Laak, and M.E. Sherman, “Using deep convolutional neural networks to identify

- and classify tumor-associated stroma in diagnostic breast biopsies,” *Modern Pathology*, vol. 31, pp. 1502–1512, June 2018.
- [21] G. Campanella, M.G. Hanna, L. Geneslaw, A. Mirafior, V. Werneck Krauss Silva, K.J. Busam, E. Brogi, V.E. Reuter, D.S. Klimstra, and T.J. Fuchs, “Clinical-grade computational pathology using weakly supervised deep learning on whole slide images,” *Nature Medicine*, vol. 25, pp. 1301–1309, July 2019.
 - [22] B. Ehteshami Bejnordi, M. Veta, P. Johannes van Diest, B. van Ginneken, N. Karssemeijer, G. Litjens, J. A. W. M. van der Laak, M. Hermesen, Q. F. Manson, M. Balkenhol, O. Geessink, N. Stathonikos, M. C. van Dijk, P. Bult, F. Beca, A. H. Beck, D. Wang, A. Khosla, R. Gargeya, H. Irshad, A. Zhong, Q. Dou, Q. Li, H. Chen, H.-J. Lin, P.-A. Heng, C. Hass, E. Bruni, Q. Wong, U. Halici, M. U. Oner, R. Cetin-Atalay, M. Berseth, V. Khvatkov, A. Vylegzhanin, O. Kraus, M. Shaban, N. Rajpoot, R. Awan, K. Sirinukunwattana, T. Qaiser, Y.-W. Tsang, D. Tellez, J. Annuscheit, P. Hufnagl, M. Valkonen, K. Kartasalo, L. Latonen, P. Ruusuvaari, K. Liimatainen, S. Albarqouni, B. Mungal, A. George, S. Demirci, N. Navab, S. Watanabe, S. Seno, Y. Takenaka, H. Matsuda, H. Ahmady Phoulady, V. Kovalev, A. Kalinovskiy, V. Li-auchuk, G. Bueno, M. M. Fernandez-Carrobles, I. Serrano, O. Deniz, D. Racoceanu, and R. Venancio, “Diagnostic assessment of deep learning algorithms for detection of lymph node metastases in women with breast cancer,” *JAMA*, vol. 318, no. 22, pp. 2199–2210, December 2018.
 - [23] P. Bandi, O. Geessink, Q. Manson, M. van Dijk, M. Balkenhol, M. Hermesen, B. Ehteshami Bejnordi, B. Lee, K. Paeng, A. Zhong, Q. Li, F. G. Zanjani, S. Zinger, K. Fukuta, D. Komura, V. Ovtcharov, S. Cheng, S. Zeng, J. Thagaard, A. B. Dahl, H. Lin, H. Chen, L. Jacobsson, M. Hedlund, M. Cetin, E. Halici, H. Jackson, R. Chen, F. Both, J. Franke, H. Kusters-Vandeveld, W. Vreuls, P. Bult, B. van Ginneken, J. van der Laak, and G. Litjens, “From detection of individual metastases to classification of lymph node status at the patient level: the camelyon17 challenge,” *IEEE Transactions on Medical Imaging*, vol. 28, no. 2, pp. 550–560, February 2019.
 - [24] D. Wang, A. Khosla, R. Gargeya, H. Irshad, and A. H. Beck, “Deep learning for identifying metastatic breast cancer,” *arXiv preprint arXiv:1606.05718*, June 2016.
 - [25] Y. Liu, K. Gadepalli, M. Norouzi, G. E. Dahl, T. Kohlberger, A. Boyko, S. Venugopalan, A. Timofeev, P. Q. Nelson, G. S. Corrado, J. D. Hipp, L. Peng, and M. C. Stumpe, “Detecting cancer metastases on gigapixel pathology images,” *arXiv preprint arXiv:1703.02442*, March 2017.
 - [26] B. Lee and K. Paeng, “A robust and effective approach towards accurate metastasis detection and pN-stage classification in breast cancer,” *Proceedings of the International Conference on Medical Image Computing and Computer-Assisted Intervention*, pp. 841–850, September 2018, Granada, Spain.
 - [27] M. Kohl, C. Walz, F. Ludwig, S. Braunewell, and M. Baust, “Assessment of breast cancer histology using densely connected convolutional networks,” *Proceedings of the International Conference Image Analysis and Recognition*, pp. 903–913, June 2018, Povia de Varzim, Portugal.
 - [28] I. Kone and L. Boulmane, “Hierarchical ResNeXt models for breast cancer histology image classification,” *Proceedings of the International Conference Image Analysis and Recognition*, pp. 796–803, June 2018, Povia de Varzim, Portugal.
 - [29] L. Hou, D. Samaras, T.M. Kurc, Y. Gao, J.E. Davis, and J.H. Saltz, “Patch-based convolutional neural network for whole slide tissue image classification,” *Proceedings of the IEEE Conference on Computer Vision and Pattern Recognition*, pp. 2424–2433, June 2016, Las Vegas, NV.
 - [30] N. Otsu, “A threshold selection method from gray-level histograms,” *IEEE Transactions on Systems, Man, and Cybernetics*, vol. 9, no. 1, pp. 62–66, January 1979.
 - [31] S. Mehta, E. Merca, J. Bartlett, D. Weaver, J. Elmore, and L. Shapiro, “Learning to segment breast biopsy whole slide images,” *Proceedings of the IEEE Winter Conference on Applications of Computer Vision*, pp. 663–672, March 2018, Lake Tahoe, NV.
 - [32] A. Agarwalla, M. Shaban, and N.M. Rajpoot, “Representation-aggregation networks for segmentation of multi-gigapixel histology images,” *arXiv preprint arXiv:1707.08814*, July 2017.
 - [33] M. Shaban, R. Awan, M.M. Fraz, A. Azam, D. Snead, and N.M. Rajpoot, “Context-aware convolutional neural network for grading of colorectal cancer histology images,” *arXiv preprint arXiv:1907.09478*, July 2019.
 - [34] F. Gu, N. Burlutskiy, M. Andersson, and L. K. Wilen, “Multi-resolution networks for semantic segmentation in whole slide images,” *Proceedings of the Computational Pathology and Ophthalmic Medical Image Analysis at the International Conference on Medical Image Computing and Computer-Assisted Intervention*, pp. 11–18, September 2018, Granada, Spain.
 - [35] H. Tokunaga, Y. Teramoto, A. Yoshizawa, and R. Bise, “Adaptive weighting multi-field-of-view cnn for semantic segmentation in pathology,” *Proceedings of the IEEE Conference on Computer Vision and Pattern Recognition*, pp. 12597–12606, June 2019, Long Beach, CA.
 - [36] J.M. Bokhorst, H. Pinckaers, P. van Zwam, I. Nagtegaal, J. van der Laak, and F. Ciompi, “Learning from sparsely annotated data for semantic segmentation in histopathology images,” *Proceedings of the International Conference on Medical Imaging with Deep Learning*, pp. 84–91, July 2019, London, United Kingdom.
 - [37] C. Fu, D.J. Ho, S. Han, P. Salama, K.W. Dunn, and E.J. Delp, “Nuclei segmentation of fluorescence microscopy images using convolutional neural networks,” *Proceedings of the IEEE International Symposium on Biomedical Imaging*, pp. 704–708, April 2017, Melbourne, Australia.
 - [38] A. Paszke, S. Gross, S. Chintala, G. Chanan, E. Yang, Z. DeVito, Z. Lin, A. Desmaison, L. Antiga, and A. Lerer, “Automatic differentiation in PyTorch,” *Proceedings of the Autodiff Workshop at Neural Information Processing Systems*, pp. 1–4, December 2017, Long Beach, CA.
 - [39] M. Buda, A. Maki, and M.A. Mazurowski, “A systematic study of the class imbalance problem in convolutional neural networks,” *Neural Networks*, vol. 106, pp. 249–259, October 2018.